International Journal of Solids and Structures 47 (2010) 2131–2142

Contents lists available at ScienceDirect

International Journal of Solids and Structures

journal homepage: www.elsevier.com/locate/ijsolstr

Micromechanical theoretical and computational modeling of energy dissipation due to nonlinear vibration of hard ceramic coatings with microstructural recursive faults

Rashid K. Abu Al-Rub [a,*], Anthony N. Palazotto [b]

[a] Zachry Department of Civil Engineering, Texas A&M University, College Station, TX 77843, USA
[b] Department of Aeronautics and Astronautics, Air Force Institute of Technology, WPAFB, OH 45433-7765, USA

ARTICLE INFO

Article history:
Received 19 August 2009
Received in revised form 19 February 2010
Available online 19 April 2010

Keywords:
Energy dissipation
Nonlinear damping
Cohesive zone modeling
Internal friction
Damage
Thermal barrier coatings

ABSTRACT

Engine failures due to high-cycle fatigue during severe dynamic vibration have cost the US Air Force an estimated $400 million dollars per year over the past two decades. Therefore, structural materials that exhibit high damping capacities are desirable for mechanical vibration suppression and acoustic noise attenuation. Few experimental studies suggested that hard ceramic coatings, which are commonly used as thermal barrier coatings (TBCs) to protect engine components from high temperatures and corrosion, can also serve as passive dampers due to their unique microstructure which consists of several layers of splats with inter- and intra-microstructural recursive faults (micro-cracks). Therefore, the focus of this study is on the development of a fundamental understanding of the unique microstructural features and mechanisms responsible for this observed energy dissipation in ceramic coatings under nonlinear vibration through the development of a micromechanical computational framework. Inter- and intra-fatigue damage and internal friction is simulated through the development of thermodynamic-based nonlinear cohesive laws that consider interfacial degradation, debonding, plastic sliding, and Coulomb/contact friction between the interfaces of microstructural faults. Representative volume element-based micromechanical simulations are conducted in order to assess the main micromechanical mechanisms responsible for the experimentally observed nonlinear (amplitude- and frequency-dependent) damping in plasma sprayed hard ceramic coatings. It is concluded that the major part of energy dissipation is achieved through contact friction which results from sliding of the splat interfaces along the microstructural recursive faults. Energy dissipation due to progressive decohesion and evolution of new micro-cracks is not that significant as compared to energy dissipated due to increased friction from existing and new created faults. Therefore, internal friction is the main mechanism that makes TBCs effective dampers.

1. Introduction

Engine failures due to high-cycle fatigue during severe dynamic vibration have cost the US Air Force an estimated $400 million dollars per year over the past two decades (Blackwell et al., 2007). Therefore, structural materials that exhibit high damping capacities are desirable for mechanical vibration (which may lead to fatigue failure) suppression and acoustic noise (which may lead to health concerns) attenuation. Therefore, it is of great importance in many engineering problems to reduce the vibratory stresses so that the life of a structural component can be extended (Patel and Palazotto, 2004). Vibratory stresses can be reduced through various frictional techniques that are based either on structural damping (active) or material damping (passive) processes. The focus of this research is on material damping and internal energy dissipation mechanisms. Damping is defined here as the internal material make-up of a substance which absorbs or dissipates energy placed upon the volume of material considered. All materials show some inherent damping capabilities due to internal friction and other microstructural deformation mechanisms such as micro-cracks evolution. This internal friction is a function of the material microstructural features, strain, stress, temperature, and frequency. Unfortunately, damping and integrity (ductility and strength) often have opposite requirements. For example, metals and ceramics are stiff but with lower damping capacities as compared to viscoelastic polymers that are soft at high temperatures but exhibit high damping behavior (see Fig. 1). Therefore, ceramic materials as opposed to polymeric materials are commonly used as

* Corresponding author. Tel.: +1 979 862 6603; fax: +1 979 845 6554.
E-mail addresses: rabualrub@civil.tamu.edu, rashedkamel@yahoo.com (R.K. Abu Al-Rub).

0020-7683/$ - see front matter © 2010 Elsevier Ltd. All rights reserved.
doi:10.1016/j.ijsolstr.2010.04.016

Nomenclature

Θ	interatomic potential function
Θ_o	fracture energy
λ	atomic separation
λ_o	atomic equilibrium separation at maximum potential energy
λ_{cr}	atomic critical separation at maximum interaction force
B^+, B^-	positive and negative sides of an interface
$\hat{\mathbf{e}}_1$, $\hat{\mathbf{e}}_2$, $\hat{\mathbf{e}}_3$	unit vectors
$\mathbf{n}$	normal to the interface
$\boldsymbol{\delta}$, $\boldsymbol{\delta}_N$, $\boldsymbol{\delta}_T$	total, normal, and tangential displacement jumps across the interface
$\boldsymbol{\delta}_T^e$, $\boldsymbol{\delta}_T^p$	elastic and plastic tangential displacement jumps
$\mathbf{t}$, $\mathbf{t}_N$, $\mathbf{t}_T$	total, normal, and tangential conjugate tractions
$t_T = \sqrt{\mathbf{t}_T \cdot \mathbf{t}_T}$	effective tangential traction
Ψ^B and Ψ^I	bulk and interfacial free energy densities
Φ	cohesive free energy per unit surface area of the fault
ϕ, D_N, and D_T	bulk, tensile, and shear damage densities
$\mathbf{C}^e$ and $\mathbf{E}^e$	right Cauchy–Green elastic strain tensor and the Lagrange elastic strain tensor
$\mathbf{F}^e$	elastic part of the deformation gradient
γ_T^p	effective tangential plastic separation due to sliding
$\mathbf{S}$	elastic stress tensor
s_T	scalar internal variable that represents the deformation resistance for sliding
X_T	backstress which introduces kinematic hardening
Y, Y_N and Y_T	bulk, tensile, and shear damage forces
Π	rate of energy dissipation due to damage growth, decohesion, and friction
Π^B	rate of energy dissipation due to bulk damage growth
ξ	rate of energy dissipation due to interfacial decohesion, plastic sliding, and friction
G and κ	shear and bulk elastic moduli
$K_N > 0$ and $K_T > 0$	normal and tangential elastic moduli of the interface
δ_N^o and δ_T^o	normal and tangential separations at which interfacial damage starts
δ_N^f and δ_T^f	normal and tangential separations at which full decohesion occurs
f_T^p	sliding yield surface at the interface
μ	kinetic friction coefficient of the interface
$\mathbf{m}_T$	direction of sliding
h	hardening/softening modulus of the interface
θ	phase- or loss-angle
ω	loading frequency
ε_0	applied strain-amplitude
E' and E''	storage and loss moduli

thermal barrier coatings (TBCs) to protect engine components from high temperatures and corrosion. In fact, recent research have indicated that ceramic TBCs can also provide some degree of vibration damping (Shipton and Patsias, 2003; Patsias et al., 2004; Tassini et al., 2006, 2007; Blackwell et al., 2007; Reed, 2007; Reed et al., 2007; Lauwagie et al., 2008; Pearson, 2008). However, constitutive modeling of this damping has been very limited in the literature due to the complex nonlinear damping behavior of these TBCs and due to the absence of a microstructural understanding of the origin of such nonlinear damping behavior. Therefore, the focus of this research is on the development of a modeling technique that can be used in predicting the main energy dissipative mechanisms that are responsible for nonlinear damping behavior of TBCs. Such modeling can ultimately be used in guiding the design of TBCs as vibration dampers in hot and cold engine sections.

Generally, the majority of TBCs are deposited using either Air Plasma Spraying (APS) or Electron Beam Physical Vapor Deposition (EBPVD) (Pawlowski, 1995). The main difference between these two methods, in terms of the coating's microstructure they produce, is that APS form splat or lamellae microstructure whereas EBPVD form columnar microstructure (see Tassini et al. (2007) for microscopic images). Although the current micromechanical modeling approach is intended for predicting the nonlinear damping response of TBCs produced by APS or EBPVD techniques, the focus of this study is on TBCs produced by the APS method. Damping treatment through the use of plasma sprayed ceramic coatings such as magnesium aluminate spinel ($MgO + Al_2O_3$ or mag spinel) and yttria-stabilized zirconia (YSZ) have received a reasonable amount of attention in turbine engine blades due to their ease of integration and cost of application, and also due to surrounding conditions in a turbine engine such as high operating temperatures that limit the use of, for example, highly nonlinear viscoelastic materials such as polymers (Reed, 2007). However, during several experimental studies, it has become apparent that *many ceramic coating materials display strain- or amplitude-dependent (i.e. nonlinear) damping and stiffness behavior*. This dependency has been reported first by Cross et al. (1973) about four decades ago and rediscovered by Patsias and co-workers (Shipton and Patsias, 2003; Patsias et al., 2004; Tassini et al., 2006, 2007) and Palazotto and co-workers (Ivancic, 2003; Ivancic and Palazotto, 2005; Blackwell et al., 2007; Reed, 2007; Reed et al., 2007; Pearson, 2008), where plasma sprayed ceramic coatings on metal substrates were investigated for damping capacity. This nonlinear behavior has resulted in numerous problems with regard to accurately characterizing and modeling these materials. Therefore, before a hard coating can be included into the design and analysis phase of a new turbine engine, its damping behavior should be fully understood in an analytical sense. Without a reasonable constitutive model for the coated material, it is difficult to accurately design a component that includes a hard coating. Moreover, there has been very little emphasis placed on the development of an effective micromechanical constitutive model that can explain the damping characteristics of hard coatings based on the physical insights from the few experimental studies and microstructural characterizations that exist in the literature on the nonlinear damping of thermal barrier

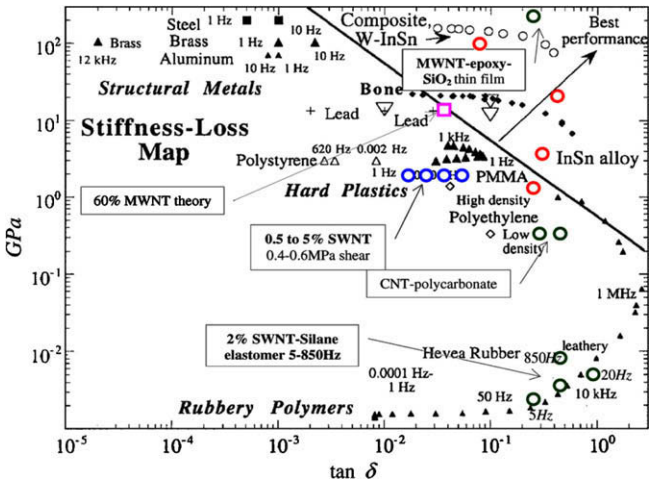

Fig. 1. Stiffness-damping map (after Lakes (1998)).

ceramic coatings (e.g. Shipton and Patsias, 2003; Patsias et al., 2004; Reed, 2007; Reed et al., 2007; Pearson, 2008; Torvik, 2009). To the authors' best knowledge, there have been only two attempts to model the nonlinear damping behavior of plasma sprayed TBCs. One by Reed (2007) and the other by Tassini et al. (2007), where both have used the Iwan (1966) spring-slider-mass analytical model in which energy dissipation is attributed only to internal friction. The Iwan (1966) model is based on the idea that as the material is loaded to greater and greater levels, more and more sliders begin to slip and the stiffness of the material continues to decrease until the point at which all the sliders have slipped. However, this analytical model cannot be used to guide the microstructural design of TBCs with optimized performance and high levels of energy dissipation. Moreover, it cannot explore the fundamental microstructural deformation mechanisms that are responsible for the experimentally observed nonlinear damping of TBCs. To the authors' best knowledge, there have been no micromechanical computational modeling of the nonlinear damping behavior of plasma sprayed ceramic coatings until the present work. Thus, the focus of this research is on the development of such a model that can effectively predict the energy dissipation mechanisms responsible for the observed nonlinear damping in hard ceramic TBCs. The objectives of this study are: (1) development of a thermodynamic-based micromechanical cohesive zone model that explicitly models the ceramic coating's microstructure, fatigue damage, decohesion, and interfacial sliding and contact friction between the interfaces of pre-existing and evolving microstructural faults or micro-cracks; (2) development of a finite element representative volume element (RVE) model with representative distributions of splats (the main building blocks of the microstructure of plasma sprayed ceramic coatings) and microstructural faults; (3) evaluate separately the energy dissipation due to decohesion and micro-cracks evolution, and energy dissipation due to plastic sliding and Coulomb/contact friction; and (4) evaluate the dependence of storage modulus and loss modulus on deformation amplitudes and excitation frequencies. Therefore, achieving the aforementioned objectives will lead to exploring the main deformation mechanisms that are responsible for energy dissipation and nonlinear damping in plasma sprayed hard ceramic coatings. Ultimately, such understanding will yield crucial recommendations for tweaking the microstructure of TBCs for high levels of vibration energy absorption and enhanced damping capacities, but without affecting or sacrificing the main functional performance of the ceramic coating.

Notation. Hereafter, $(\cdot)$ and $(:)$ stand for tensor contraction (i.e. $\mathbf{a}\cdot\mathbf{b}=a_ib_i$ and $\mathbf{A}:\mathbf{B}=A_{ij}B_{ij}$), $\mathrm{tr}\mathbf{A}=A_{kk}$ for trace of a second-order tensor, the superimposed dot $(\dot{\cdot})$ indicates the differentiation with respect to time t, and the symbol $\otimes$ indicates the dyadic product of two vectors such that $\mathbf{a}\otimes\mathbf{b}=a_ib_j$.

2. Micromechanical damping mechanisms

Passive damping in materials can be attributed to several stationary and evolved microstructural factors such as individual constituents as in composites, interfacial effects (e.g. grain boundaries, film–substrate interface, inclusion/phase interface, and free surfaces of cracks), vacancies and interstitial atoms, dislocations in metals, nano-twins (i.e. twin sizes on the order to tens to few hundreds of nanometers), phase transformation, magnetostriction, ferroelasticity, piezoelectricity, etc. The size of the microstructural features could also have a significant effect on damping capacities of materials.

It is believed through few experimental characterization results that the main damping mechanism in hard ceramic coatings could be the internal friction due to relative movement of the coating's internal micro-cracks (micro-faults or cohesive micro-cracks), micro-cracks' nucleation and growth, and distribution of a high density of microstructural building flat-like splats (see Fig. 2(b) and (c)) as argued by Shipton and Patsias (2003) and Pearson (2008). These splats are formed by the air plasma spray fabrication technique through rapid solidification of molten droplets after impacting a metallic substrate surface (see Fig. 2(a)) such that interconnected networks of micro-pores and micro-cracks are generated in the material microstructure (see Fig. 2(b) and (c)). It can be seen from Fig. 2(b) and (c) that several families of defects are distinguished: (1) inter-splat micro-faults or cohesive micro-cracks between different splats; (2) irregular intra-splat micro-faults inside the splats; (3) large irregular micro-voids between splats; and (4) small micro-voids inside the splats. Splat size (on the order of 100–200 μm in diameters and 2–10 μm in thickness), splat boundary axis angle in relation to the applied strain, and parallelism of splat boundary and vertical columnar micro-cracks (i.e. micro-faults orientations and density) all could have a profound effect on damping behavior of TBCs. Therefore, it is expected that damping can be increased by optimizing defect interface friction, defect boundary bond strength, splat geometry and size, and defect density. Fig. 2(b) and (c) shows the microstructure of recursive micro-fault patterns in two commercial ceramic TBCs that if internal friction and micro-deformation of these micro-faults simulated explicitly as an important dissipation mechanism in hard ceramic coatings, valuable insights about internal microstructural damping mechanisms could be revealed and assessed. This is the main goal of the proposed micromechanical modeling where a nonlinear elastic–plastic-damage cohesive zone constitutive model will be formulated based on the laws of thermodynamics. Fig. 3 shows a schematic for the micromechanical procedure used here in simulating the nonlinear damping behavior observed in hard ceramic coatings. This framework is described in the subsequent sections.

3. Micromechanical nonlinear cohesive interface model

In order to gain fundamental insight into the nonlinear damping microstructural mechanisms in hard ceramic coatings, a micromechanical nonlinear cohesive model, which explicitly takes into consideration decohesion, sliding, and internal friction between splats along the pre-existing and evolving microstructural recursive faults or micro-cracks, will be developed based on the laws of thermodynamics and implemented into the well-known finite element code ABAQUS (2004). Cohesive interface modeling of fracture and damage started about 50 years ago with the work of Barenblatt (1959) and Dugdale (1960). In recent years, cohesive interface models have been widely used to numerically simulate fracture initiation and growth by the finite element method (e.g. Needleman, 1990; Xu and Needleman, 1994; Camacho and Ortiz, 1996). For a recent review see Hutchinson and Evans (2000) and Chaboche (2003).

The novel feature of cohesive zone modeling at the continuum level is the average representation of particle debonding at the atomistic level as a function of the atomic separation distance λ between two rows of atoms (two fractured surfaces at the continuum level). The general shape of an atomistic potential (e.g. Lennard-Jones potential), Θ, is shown in Fig. 4 which has a maximum at an atomic equilibrium separation, λ_o, since the interaction force (i.e. the derivative of the potential function $\partial\Theta/\partial\lambda$) must be attractive at larger distances and repulsive at smaller distances. The work to complete dissociation of bond (i.e. fracture energy), Θ_f, is the area under the interaction force curve as shown in Fig. 4. When the separation distance between particles reaches a critical value, λ_{cr}, the interaction reaches its maximum

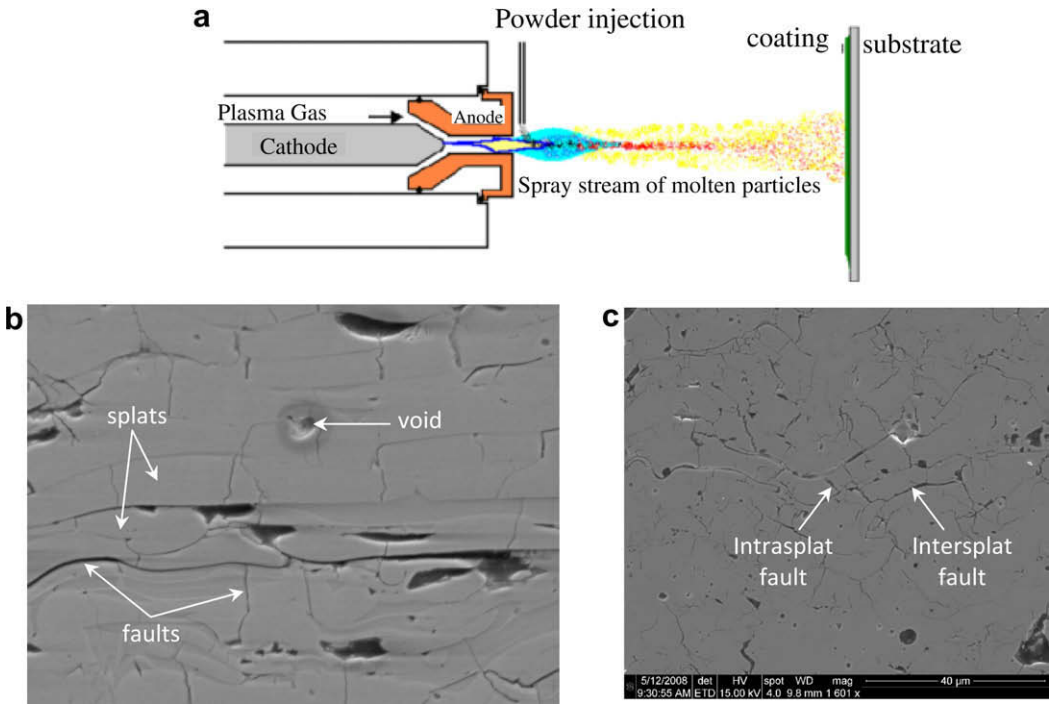

Fig. 2. Air plasma spray technique and the deposited coating's microstructure. (a) Schematic of the air plasma spray technique and microstructural defects (voids and cracks) in (b) MgAl spinel (after Shipton and Patsias (2003)) and (c) yttria-stabilized zirconia (after Pearson (2008)) hard ceramic coatings with inherent microstructural distributed faults between splats.

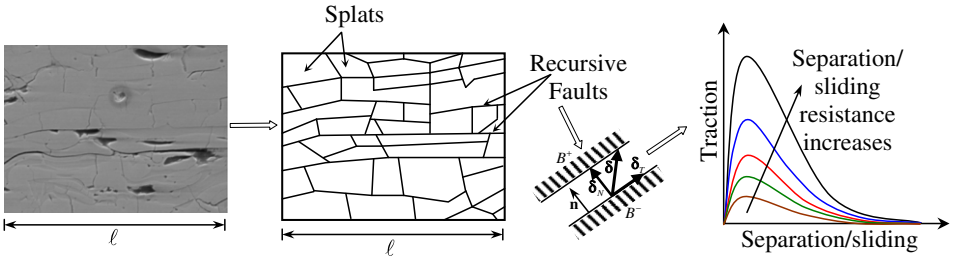

Fig. 3. Microstructural modeling of recursive faults in a representative volume element using the cohesive elements.

and starts decreasing as the separation increases until complete decohesion. Therefore, cohesive zone modeling bridges the gap between interatomic bonding and continuum cohesive failure.

Moreover, cohesive interface models play an intermediate role between fracture mechanics and continuum damage mechanics. Typically, a cohesive interface is introduced in a finite element discretization of the problem through the use of special interface elements which obey a nonlinear interface traction–separation or traction–sliding or slipping constitutive relations that provide a phenomenological description for the complex microscopic processes that lead to the formation of new traction-free crack faces. The loss of cohesion, and thus of crack nucleation and extension, occurs by the progressive decay of interface tractions. The interface traction–separation relation usually includes a cohesive strength and a cohesive work-to-fracture (i.e. interfacial fracture energy of the material). Once the local strength and work-to-fracture criteria across an interface are met, decohesion occurs naturally across the interface, and traction-free cracks form and propagate along element boundaries.

In the following sections, a thermodynamic-based cohesive elastic–plastic-damage model that explicitly predicts the distributed micro-damage evolution and interfacial slipping (friction) in hard ceramic coatings is developed. The objective of the proposed cohesive model is to provide a unified framework for explicit modeling of internal friction and fatigue damage in hard ceramic coatings through modeling the coating's microstructure and interfacial behavior between splats. The loss of cohesion, and thus of interfacial sliding and micro-crack nucleation and growth, occurs by the progressive decay of interface tractions. Moreover, the model accounts for the elastic-damage behavior of the matrix, fault nucleation, and the cohesive and frictional behavior of the faults.

3.1. Interfacial tractions, jumps, and sliding

Consider two blocks B^+ and B^- separated by an interface $\boldsymbol{I}$ (Fig. 5(a)). Let $\hat{\mathbf{e}}_1$, $\hat{\mathbf{e}}_2$, and $\hat{\mathbf{e}}_3$ be an orthogonal triad, with $\hat{\mathbf{e}}_1$ aligned with the normal $\boldsymbol{n}$ to the interface, and $\hat{\mathbf{e}}_2$ and $\hat{\mathbf{e}}_3$ in the tangent plane at the point of the interface under consideration. Let $\boldsymbol{\delta}$ denote the displacement jump across the interface, and $\boldsymbol{t}$ the conjugate traction. One can also decompose $\boldsymbol{\delta}$ into a normal component, δ_N, along $\hat{\mathbf{e}}_1$ and tangential components, δ_T, along $\hat{\mathbf{e}}_2$ and $\hat{\mathbf{e}}_3$, where positive δ_N corresponds to increasing separation. Similarly, one can decompose the traction $\mathbf{t}$ into a normal component, $\mathbf{t}_N$, and tangential components, $\mathbf{t}_T$. Therefore, one can write

$$\mathbf{t} = \mathbf{t}_N + \mathbf{t}_T, \quad \boldsymbol{\delta} = \boldsymbol{\delta}_N + \boldsymbol{\delta}_T \tag{1}$$

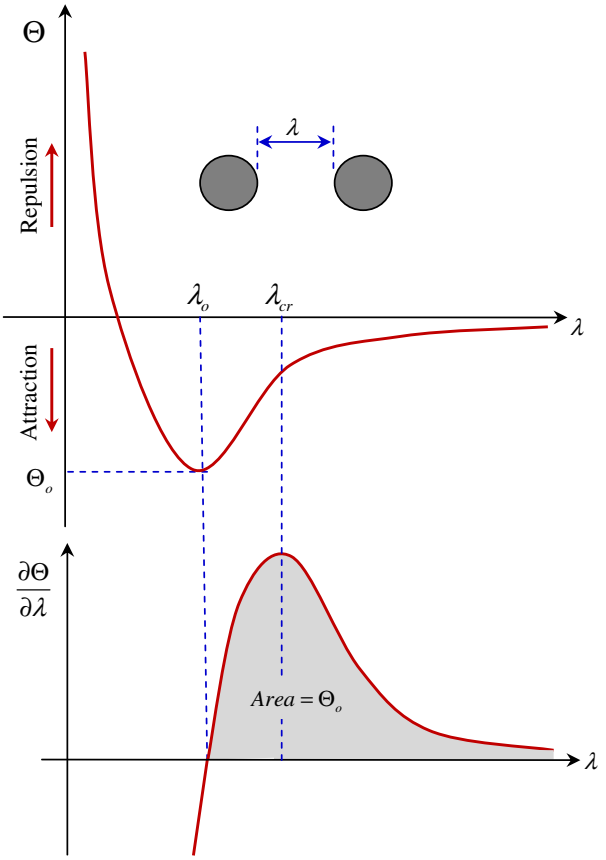

Fig. 4. Atomistic representation of cohesive zone modeling showing the shape of atomic potential energy and the corresponding interaction–separation curve.

Also, one can write

$$\mathbf{t}_N = (\mathbf{n}\otimes\mathbf{n})\mathbf{t} = (\mathbf{t}\cdot\mathbf{n})\mathbf{n} = t_N\mathbf{n}, \quad \mathbf{t}_T = (\mathbf{1}-\mathbf{n}\otimes\mathbf{n})\mathbf{t} = \mathbf{t} - t_N\mathbf{n} \tag{2}$$

where t_N represents the normal stress at the interface. One can denote the magnitude of the tangential traction vector $\mathbf{t}_T$ by $t_T = \sqrt{\mathbf{t}_T\cdot\mathbf{t}_T}$ and call it the effective tangential traction or simply the shear stress.

Similarly, one can write

$$\boldsymbol{\delta}_N = (\mathbf{n}\otimes\mathbf{n})\boldsymbol{\delta} = (\boldsymbol{\delta}\cdot\mathbf{n})\mathbf{n} = \delta_N\mathbf{n}, \quad \boldsymbol{\delta}_T = (\mathbf{1}-\mathbf{n}\otimes\mathbf{n})\boldsymbol{\delta} = \boldsymbol{\delta} - \delta_N\mathbf{n} \tag{3}$$

where δ_N represents the magnitude of the normal separation at the interface. Also, one can denote the magnitude of the tangential separation vector $\boldsymbol{\delta}_T$ by $\delta_T = \sqrt{\boldsymbol{\delta}_T\cdot\boldsymbol{\delta}_T}$ and call it the effective tangential separation.

Let us assume the possibility of sliding before complete interfacial decohesion (Chaboche et al., 2001). Therefore, one can split the tangential displacement jump into elastic, $\boldsymbol{\delta}_T^e$, and plastic, $\boldsymbol{\delta}_T^p$, parts similar to the classical plasticity theory (e.g. Lemaitre and Chaboche, 1990), such that:

$$\boldsymbol{\delta}_T = \boldsymbol{\delta}_T^e + \boldsymbol{\delta}_T^p \tag{4}$$

Therefore, it is assumed that the normal jump δ_N is elastic without a plastic component (i.e. $\delta_N = \delta_N^e$).

3.2. Thermodynamic restrictions

In order to derive consistent constitutive equations for the tractions $\mathbf{t}_N$ and $\mathbf{t}_T$ at the interface and the elastic-damage behavior of the bulk material between the interfaces within the laws of thermodynamics, the Helmholtz free energy density Ψ can be decomposed into a free energy in the bulk (i.e. in the ceramic splat), Ψ^B, and a free energy at the interface (i.e. in the fault), Ψ^I, such that:

$$\Psi = \underbrace{\Psi^B(\mathbf{C}^e,\phi)}_{\text{free energy in bulk}} + \underbrace{\Psi^I(\boldsymbol{\delta}_N^e,\boldsymbol{\delta}_T^e,\gamma_T^p,D_N,D_T)}_{\text{free energy at interfaces}} \tag{5}$$

where $\mathbf{C}^e = \mathbf{F}^{eT}\mathbf{F}^e$ is the right Cauchy–Green elastic deformation tensor, where $\mathbf{F}^e$ is the elastic part of the deformation gradient, ϕ is the damage density in the bulk (i.e. micro-cracks and micro-voids density within the splat), $\gamma_T^p = \int_0^t \dot{\gamma}_T^p\,dt = \int_0^t \sqrt{\dot{\boldsymbol{\delta}}_T^p\cdot\dot{\boldsymbol{\delta}}_T^p}\,dt$ is the effective tangential plastic separation due to sliding with $\dot{\boldsymbol{\delta}}_T^p$ being the rate of the tangential separations. In this paper, the superimposed dot designates derivative with respect to time. The internal state variables D_N and D_T are degradation variables of the normal and tangential cohesive strengths, respectively. According to continuum damage mechanics (e.g. Kachonov, 1958; Krajcinovic, 1983; Lemaitre, 1992), the damage variables ϕ, D_N, and D_T degrade the strength and stiffness of the bulk and interfaces and they have a range from 0 to 1, where 0 indicates no damage (or perfect cohesion) and 1 indicates fracture (or complete decohesion). $D_T = 1$ signifies that the interface has failed and is only capable of transmitting compressive and tangential tractions due to contact friction. Note that $\Psi^I = \Phi/L$, where Φ is the cohesive energy per unit fault surface area and L is a microstructural length scale parameter, which is assumed constant in this study, and could be physically interpreted as the average thickness of the splats.

One considers here a purely mechanical theory where isothermal conditions are assumed such that based on the requirement that the rate of change in the total free energy should be less than or equal to that power done by external forces (Coleman and Gurtin, 1967), one can write the second law of thermodynamic as:

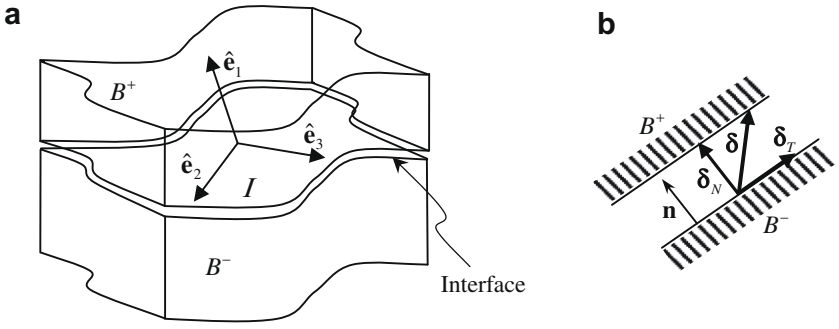

Fig. 5. (a) Schematic representation of an interface between two splats. (b) Decomposition of the opening displacement $\boldsymbol{\delta}$ into normal component $\boldsymbol{\delta}_N$ and tangential components $\boldsymbol{\delta}_T$.

$$\int_{\Gamma} \dot{\Psi}\, dV \leqslant P_{ext} \tag{6}$$

where V is the reference (initial) volume of a sub-body Γ, and P_{ext} is the external power which according to the first law of thermodynamics is equal to the internal power P_{int} (i.e. $P_{ext} = P_{int}$) such that P_{int} is defined as:

$$P_{int} = \int_{\Gamma} \left[\frac{1}{2}\mathbf{S} : \dot{\mathbf{C}}^{e} + \frac{1}{L}\mathbf{t}_{N} \cdot \dot{\boldsymbol{\delta}}_{N}^{e} + \frac{1}{L}\mathbf{t}_{T} \cdot \dot{\boldsymbol{\delta}}_{T}^{e}\right] dV \tag{7}$$

where $\boldsymbol{S}$ is the elastic stress tensor.

Substituting Eq. (7) into Eq. (6) with $P_{ext} = P_{int}$, one can write the Clausius–Duhem inequality point wise as follows:

$$\frac{1}{2}\mathbf{S} : \dot{\mathbf{C}}^{e} + \frac{1}{L}\mathbf{t}_{N} \cdot \dot{\boldsymbol{\delta}}_{N}^{e} + \frac{1}{L}\mathbf{t}_{T} \cdot \dot{\boldsymbol{\delta}}_{T}^{e} - \dot{\Psi} \geqslant 0 \tag{8}$$

Note that the Clausius–Duhem inequality gives the rate of energy dissipation per unit reference volume.

If one substitutes the time derivative of Eq. (5) into Eq. (8) along with $\Psi^{I} = \Phi/L$, the following is obtained:

$$\begin{aligned}\left(\frac{1}{2}\mathbf{S} - \frac{\partial \Psi^{B}}{\partial \mathbf{C}^{e}}\right) : \dot{\mathbf{C}}^{e} - \frac{\partial \Psi^{B}}{\partial \phi}\dot{\phi} + \frac{1}{L}\left(\mathbf{t}_{N} - \frac{\partial \Phi}{\partial \boldsymbol{\delta}_{N}^{e}}\right) \cdot \dot{\boldsymbol{\delta}}_{N}^{e} + \frac{1}{L}\left(\mathbf{t}_{T} - \frac{\partial \Phi}{\partial \boldsymbol{\delta}_{T}^{e}}\right) \\ \cdot \dot{\boldsymbol{\delta}}_{T}^{e} - \frac{1}{L}\left(\frac{\partial \Phi}{\partial \gamma_{T}^{p}}\dot{\gamma}_{T}^{p} + \frac{\partial \Phi}{\partial D_{N}}\dot{D}_{N} + \frac{\partial \Phi}{\partial D_{T}}\dot{D}_{T}\right) \\ \geqslant 0\end{aligned} \tag{9}$$

From the above expression one can define the following thermodynamic conjugate forces:

$$\mathbf{S} = 2\frac{\partial \Psi^{B}}{\partial \mathbf{C}^{e}}, \quad Y = -\frac{\partial \Psi^{B}}{\partial \varphi} \tag{10}$$

$$\mathbf{t}_{N} = \frac{\partial \Phi}{\partial \boldsymbol{\delta}_{N}^{e}}, \quad \mathbf{t}_{T} = \frac{\partial \Phi}{\partial \boldsymbol{\delta}_{T}^{e}}, \quad s_{T}^{p} = -\frac{\partial \Phi}{\partial \gamma_{T}^{p}}, \quad Y_{N} = -\frac{\partial \Phi}{\partial D_{N}}, \quad Y_{T} = -\frac{\partial \Phi}{\partial D_{T}} \tag{11}$$

where Y is the damage driving force within the bulk (i.e. within the ceramic matrix), s_T is the thermodynamic force associated with plastic sliding, and Y_N and Y_T are the normal and tangential damage driving forces at the interface. The damage forces Y, Y_N, and Y_T can be interpreted as the energy release rates (i.e. the energy required to create a unit damaged surface area) as argued by Abu Al-Rub and Voyiadjis (2003).

Substituting the thermodynamic laws in Eqs. (10) and (11) into Eq. (9), one can express the rate of energy dissipation (dissipated as heat), Π, due to micro-crack evolution in the bulk, Π^{B}, and decohesion and sliding at the interface, $\Pi^{I} = \xi/L$, as follows:

$$\Pi = \Pi^{B} + \Pi^{I} = \Pi^{B} + \frac{1}{L}\xi \geqslant 0 \tag{12}$$

where

$$\Pi^{B} = Y\dot{\phi} \geqslant 0, \quad \xi = -s_{T}^{p}\dot{\gamma}_{T}^{p} + Y_{N}\dot{D}_{N} + Y_{T}\dot{D}_{T} \geqslant 0 \tag{13}$$

One can assume the following form for the bulk Helmholtz free energy density:

$$\Psi^{B} = (1-\phi)\left[G\mathbf{E}^{e} : \mathbf{E}^{e} + \frac{1}{2}\kappa|\mathrm{tr}\mathbf{E}^{e}|^{2}\right] \tag{14}$$

where $\mathbf{E}^{e} = (\mathbf{C}^{e} - \mathbf{1})/2$ is the elastic strain tensor, G and κ are the undamaged elastic shear and bulk moduli, respectively.

Substituting Eq. (14) into Eq. (10) yields

$$\mathbf{S} = (1-\phi)(2G\mathbf{E}^{e} + \kappa \mathrm{tr}\mathbf{E}^{e}) \tag{15}$$

$$Y = G\mathbf{E}^{e} : \mathbf{E}^{e} + \frac{1}{2}\kappa|\mathrm{tr}\mathbf{E}^{e}|^{2} \tag{16}$$

The bulk damage variable φ is assumed to have the following exponential evolution equation:

$$\dot{\phi} = \frac{B}{Y_{o}} \exp\left[B\left(1 - \frac{Y}{Y_{o}}\right)\right]\dot{Y} \tag{17}$$

where Y_o is the damage threshold and B indicates the damage evolution rate. Once the damage driving force Y exceeds Y_o damage growth starts in the bulk.

3.3. Interfacial damage and decohesion

In order to derive the constitutive equations for the normal and tangential tractions, $\mathbf{t}_N$ and $\mathbf{t}_T$, in Eqs. $(11)_1$ and $(11)_2$, respectively, and the evolution equations for the normal and tangential damage forces, Y_N and Y_T, in Eqs. $(11)_4$ and $(11)_5$, respectively, one needs to postulate an analytical form for the interfacial energy $\Phi = L\Psi^{I}$ in Eq. (5). The following quadratic expression is adapted from Chaboche (2003), such that:

$$\begin{aligned}2\Phi = [\boldsymbol{\delta} - H(-\delta_{N})\boldsymbol{\delta}^{p}] \cdot \mathbf{K}^{d}(D_{N}, D_{T}) \cdot [\boldsymbol{\delta} - H(-\delta_{N})\boldsymbol{\delta}^{p}] + h \\ \times \frac{(1-D_{T})}{D_{T}} \frac{(\gamma_{T}^{p})^{2}}{\delta_{T}^{f}}\end{aligned} \tag{18}$$

where $\mathbf{K}^{d}(D_N, D_T)$ is the interfacial elastic-damaged stiffness tensor and taken to be positive definite, and h is a material hardening parameter associated with deformation resistance to sliding. $H(x)$ is the Heaviside step function such that $H = 1$ for $x \geqslant 0$ and $H = 0$ for $x < 0$. Therefore, the first term in Eq. (18) is the elastic stored energy at the interface whereas the second term is the stored energy at the interface due to sliding resistance. The Heaviside step function $H(x)$ is incorporated into the first term of Eq. (18) indicating that plastic sliding occurs only under compression (i.e. when $\delta_N < 0$).

Assuming decoupling between the normal and tangential separations, one can decompose $\mathbf{K}^{d}$ in Eq. (18) into a normal interfacial elastic-damage stiffness tensor, $\mathbf{K}_{N}^{d}$, and a tangential interfacial elastic-damage stiffness tensor, $\mathbf{K}_{T}^{d}$, such that:

$$\mathbf{K}^{d} = \mathbf{K}_{N}^{d} + \mathbf{K}_{T}^{d} \tag{19}$$

Motivated by classical continuum damage mechanics (e.g. Abu Al-Rub and Voyiadjis, 2003), the following simple expressions can be assumed for $\mathbf{K}_{N}^{d}$ and K_{T}^{d} in terms of the initial undamaged elastic counterparts, $\mathbf{K}_N$ and $\mathbf{K}_T$, and the normal and tangential damage densities D_N and D_T that degrade $\mathbf{K}_N$ and $\mathbf{K}_T$, respectively, such that:

$$\mathbf{K}_{N}^{d} = [(1-D_{N})H(\delta_{N}) + H(-\delta_{N})]\mathbf{K}_{N} \tag{20}$$

$$\mathbf{K}_{T}^{d} = [(1-D_{T})H(\delta_{N}) + H(-\delta_{N})]\mathbf{K}_{T} \tag{21}$$

where $\mathbf{K}_N = \left(K_N/\delta_N^f\right)\mathbf{n}\otimes\mathbf{n}$, $\mathbf{K}_T = \left(K_T/\delta_T^f\right)(\mathbf{1} - \mathbf{n}\otimes\mathbf{n})$ with $K_N > 0$ and $K_T > 0$ are the normal and tangential elastic (undamaged) moduli of the interface, respectively. The separations δ_N^f and δ_T^f are normal and tangential length scales, respectively, which are related to the fracture energy and the cohesive strength. $\mathbf{1}$ is the identity tensor and $\boldsymbol{n}$ is the normal to the interface. The Heaviside step function $H(x)$ is introduced in the above equation indicating that interfacial damage does not occur during compressing the interface. Therefore, interfacial damage occurs when the interface is under tension and/or shear. Note that the expressions for $\mathbf{K}_N$ and $\mathbf{K}_T$ are normalized by δ_N^f and δ_T^f, respectively, so that K_N and K_T have the units of a stress.

Substituting Eqs. $(1)_2$, (3) and (4) into Eq. (18) along with Eqs. (19)–(21), one can rewrite the expression for the interfacial energy Φ as follows:

$$2\Phi = [(1-D_N)H(\delta_N) + H(-\delta_N)]K_N\frac{(\delta_N)^2}{\delta_N^f} + [(1-D_T)H(\delta_N) + H(-\delta_N)]K_T\frac{\left[\delta_T - \gamma_T^p H(-\delta_N)\right]^2}{\delta_T^f} + h\frac{(1-D_T)}{D_T}\frac{(\gamma_T^p)^2}{\delta_T^f} \tag{22}$$

Also, one can write the expressions for the effective normal and tangential thermodynamic tractions, t_N and t_T, from Eqs. $(11)_1$ and $(11)_2$ along with Eqs. $(1)_2$, (3) and (4) as follows:

$$t_N = \frac{\partial\Phi}{\partial\delta_N^e}, \quad t_T = \frac{\partial\Phi}{\partial\delta_T^e} \tag{23}$$

Therefore, substituting Eq. (22) into Eq. (23) gives

$$t_N = [(1-D_N)H(\delta_N) + H(-\delta_N)]K_N\left(\frac{\delta_N}{\delta_N^f}\right) \tag{24}$$

$$t_T = [(1-D_T)H(\delta_N) + H(-\delta_N)]K_T\frac{\left[\delta_T - \delta_T^p H(-\delta_N)\right]}{\delta_T^f} \tag{25}$$

A schematic representation of the above traction–separation laws are shown in Fig. 6(a) and (b) for Mode I (i.e. when $\delta_T = 0$) and Mode II (i.e. when $\delta_N = 0$), respectively. The behavior under normal tension (i.e. $\delta_N > 0$) reduces Eqs. (24) and (25) to

$$t_N = (1-D_N)K_N\frac{\delta_N}{\delta_N^f}, \quad t_T = (1-D_T)K_T\frac{\delta_T}{\delta_T^f} \tag{26}$$

whereas for compression (i.e. $\delta_N < 0$), Eqs. (24) and (25) reduce to

$$t_N = K_N\frac{\delta_N}{\delta_N^f}, \quad t_T = K_T\frac{\delta_T - \delta_T^p}{\delta_T^f} \tag{27}$$

Note that the constitutive relations are similar for positive and negative tangential jumps.

Substituting Eq. (22) into Eqs. $(11)_4$ and $(11)_5$, gives the following expressions for the thermodynamic damage forces Y_N and Y_T such that:

$$Y_N = \frac{1}{2}K_N\frac{(\delta_N)^2}{\delta_N^f}, \quad Y_T = \frac{1}{2}K_T\frac{\left[\delta_T - \gamma_T^p H(-\delta_N)\right]^2}{\delta_T^f} + \frac{1}{2}\frac{h}{(D_T)^2}\frac{(\gamma_T^p)^2}{\delta_T^f} \tag{28}$$

Damage starts when the separations δ_N or δ_T exceed the critical values δ_N^o or δ_T^o, respectively (see Fig. 6). This can be considered as the interfacial damage initiation criterion. Thus, the expressions for the damage variables D_N and D_T should satisfy the conditions of $D_m = 0$ when $\delta_m = \delta_m^o$, and $D_m = 1$ when $\delta_m = \delta_m^f$, where $m = N$ for normal damage and $m = T$ for tangential damage such that the following exponential equation is postulated:

$$D_m = 1 - \frac{Y_m^o}{Y_m}\left[1 - \frac{1 - \exp\left\{-\alpha_m\left(\frac{Y_m - Y_m^o}{Y_m^f - Y_m^o}\right)\right\}}{1 - \exp(-\alpha_m)}\right] \tag{29}$$

where $\alpha_m > 0$ is a material parameter that indicates the rate of interfacial damage evolution, whereas $Y_m^o = K_m(\delta_m^o)^2/2\delta_m^f$ and $Y_m^f = K_m\delta_m^f/2$ with δ_m^o and δ_m^f are the critical separations at which damage initiates and debonding occurs, respectively (see Fig. 6). Both δ_m^o and δ_m^f are material parameters that have the dimensions of length and, therefore, they can be considered intrinsic material length scale parameters that allow one to obtain mesh-independent regularized solutions.

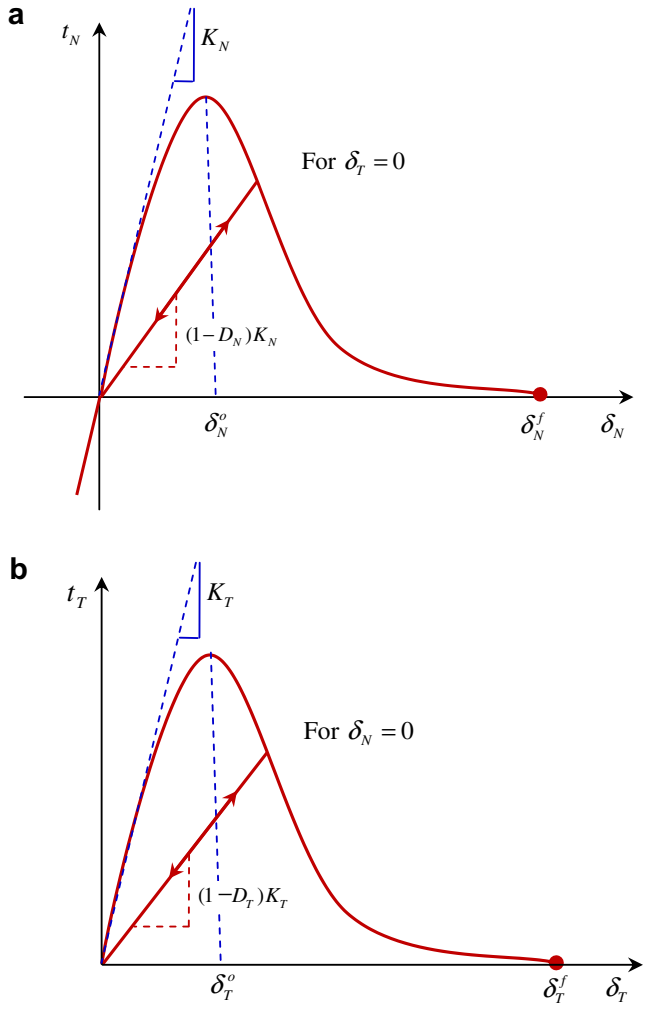

Fig. 6. Schematic of the nonlinear traction–separation responses. (a) Mode I: normal traction–normal separation response. (b) Mode II: tangential shear traction–sliding response.

3.4. Sliding and Coulomb's friction

Internal friction could be the most important dissipation mechanism in hard ceramic coatings, which will be revealed through the outlined micromechanical simulations in the next section. Therefore, one should assume that friction operates at the interfaces (faults) concurrently with cohesion. However, after complete separation, a contact/Coulomb's friction may become the sole dissipation mechanism at the faults.

Substituting Eq. (22) into the expression for the sliding thermodynamic force s_T^p in Eq. $(11)_3$ yields

$$s_T^p = t_T - h\frac{(1-D_T)}{D_T}\frac{\gamma_T^p}{\delta_T^f} = t_T - X_T \tag{30}$$

where

$$X_T = h\frac{(1-D_T)}{D_T}\frac{\gamma_T^p}{\delta_T^f} \tag{31}$$

such that the backstress X_T introduces a kinematic hardening effect during the cyclic loading with an infinite slope at the beginning (i.e. $D_T = 0$) and a decreasing hardening modulus as damage grows. Therefore, at complete decohesion (i.e. for $D_T = 1$), the sliding resistance is only due to contact friction such that $X_T = 0$ from Eq. (31) and $s_T^p = t_T$ from Eq. (30), where in this case t_T is the kinetic frictional force. This is explained in detail in the following paragraphs. Moreover, the backstress X_T introduces a memory

effect due to load reversal from tension to compression or vice versa, for example, during nonlinear vibration as in the problem considered in the current study. Hence, the accumulated plastic sliding will affect the magnitude of further plastic sliding.

Coulomb's friction or sliding plays a role during the debonding of intra- and inter-splats interfaces and contact between interfaces through using a plasticity yield-like surface as follows:

$$f_{\mathrm{T}}^{\mathrm{p}} = t_{\mathrm{T}} - \mu\langle -t_{\mathrm{N}}\rangle - X_{\mathrm{T}} \leqslant 0 \tag{32}$$

where μ is the friction coefficient between the splats' interfaces, X_{T} is given in Eq. (31), and $\langle\cdot\rangle$ denotes the Macauley bracket.

Analogous to classical plasticity theory, the evolution of plastic sliding rate, $\dot{\boldsymbol{\delta}}_{\mathrm{T}}^{\mathrm{p}}$, can be computed using the following associative flow rule:

$$\dot{\boldsymbol{\delta}}_{\mathrm{T}}^{\mathrm{p}} = \dot{\gamma}_{\mathrm{T}}^{\mathrm{p}}\mathbf{m}_{\mathrm{T}}, \quad \mathbf{m}_{\mathrm{T}} = \frac{\partial f_{\mathrm{T}}^{\mathrm{p}}}{\partial \mathbf{t}_{\mathrm{T}}} = \frac{\mathbf{t}_{\mathrm{T}}}{t_{\mathrm{T}}} \tag{33}$$

such that the loading/unloading conditions can be expressed as

$$f_{\mathrm{T}}^{\mathrm{p}} \leqslant 0, \quad \dot{\gamma}_{\mathrm{T}}^{\mathrm{p}} \geqslant 0, \quad \dot{\gamma}_{\mathrm{T}}^{\mathrm{p}} f_{\mathrm{T}}^{p} = 0 \tag{34}$$

These conditions can be used in evaluating $\dot{\gamma}_{\mathrm{T}}^{\mathrm{p}}$. Moreover, the meaning of these conditions is indicated next.

Fig. 7 shows the behavior of plastic sliding under normal compression. In the tangential model, when $t_{\mathrm{N}} < 0$ (i.e. compressive loading), the proposed sliding model behaves like a classical plasticity model with linear kinematic hardening, in which the yield limit is given by $\mu|t_{\mathrm{N}}|$ such that when $|t_{\mathrm{T}}| < \mu|t_{\mathrm{N}}|$ no sliding occurs. The hardening modulus, which is initially infinite, decreases with damage and vanishes at complete separation. After complete decohesion, an increased resistance due to contact/Coulomb's friction is anticipated such that the non-vanishing tangential traction equals $\mu\langle -t_{\mathrm{N}}\rangle$. Therefore, under compressive loading, one can have three possibilities according to the proposed sliding model: (1) neither the damage initiation and plastic slipping criteria are satisfied such that the interfacial deformation behavior is purely elastic with the initial stiffness is given by K_{T} (Eq. $(27)_2$); (2) the tangential damage does not grow but the Coulomb's sliding condition is satisfied such that sliding occurs with $\dot{\gamma}_{\mathrm{T}}^{\mathrm{p}} \neq 0$; (3) the tangential decohesion progresses as the damage parameter D_{T} increases and at the same time $f_{\mathrm{T}}^{\mathrm{p}} = 0$ is imposed such that the plastic sliding $\delta_{\mathrm{T}}^{\mathrm{p}}$ increases. On the other hand, in the case of normal tension (i.e. $\delta_{\mathrm{N}} > 0$) and satisfaction of the plasticity condition in Eq. (32), one can evaluate the plastic sliding by substituting Eqs. $(26)_2$ and (31) into Eq. (32) such that $\gamma_{\mathrm{T}}^{\mathrm{p}} = D_{\mathrm{T}}(K_{\mathrm{T}}/h)\delta_{\mathrm{T}}$. Therefore, in the case of tension-shear condition, the tangential response can be considered as either: (1) an elastic-damaging one with a decreasing tangential modulus as in Eq. $(26)_2$; or (2) an elastoplastic-damage model with a zero yield limit and linear kinematic hardening that decreases with damage.

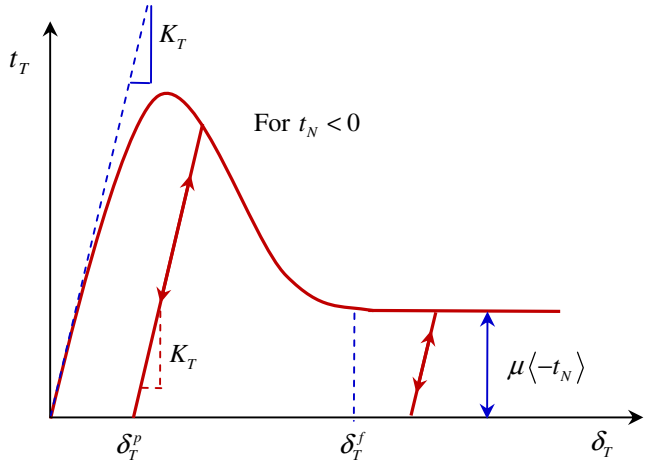

Fig. 7. Schematic behavior of plastic sliding under tangential loading and compression normal traction (i.e. $t_{\mathrm{N}} < 0$).

4. Micromechanical simulations

The proposed constitutive model has been implemented numerically in the well-known commercial finite element code ABAQUS as a user material subroutine UMAT in order to simulate energy dissipation due to decohesion, fault friction, sliding, and crack evolution and propagation in hard ceramic coatings when subjected to vibrations as demonstrated in Fig. 8. The RVE includes a random distribution of inter-splat and intra-splat microstructural faults taken to represent the microstructure of the SEM image in Fig. 3. The effect of micro-voids is neglected in these RVE simulations and will be considered in a future work. In fact, it is anticipated that the effect of the evolution of micro-voids will not be significant on the energy dissipation as compared to that from micro-cracks. As shown in Fig. 8, the RVE is loaded with harmonic deformations under different strain-amplitudes, ε_{o}, and frequencies, ω, such that the stationary stress response is evaluated in terms of the dynamic modulus and the phase-angle, θ, or, equivalently, in terms of the storage modulus, $E' = (\sigma_{\mathrm{o}}/\varepsilon_{\mathrm{o}})\cos\theta$, and the loss modulus, $E'' = (\sigma_{\mathrm{o}}/\varepsilon_{\mathrm{o}})\sin\theta$. The storage modulus is equivalent to the coating modulus. Also, Fig. 8 shows the FE mesh where cohesive zone elements are inserted at the interfaces between and within the splats. In order to simulate the damping response of a free-free beam, so that any artificial energy dissipation due to boundary constraining is avoided, symmetrical boundary conditions are imposed on the RVE such that the bottom boundary of the RVE is constrained from motion in the vertical direction whereas the left boundary of the RVE is constrained from motion in the horizontal direction. The strain-amplitude is applied at the right boundary of the RVE. The problem is solved assuming plane stress conditions.

The focus of the current numerical simulations is on estimating the energy dissipated due to micro-damage and plastic sliding and Coulomb friction, and on evaluating the change of the storage and loss moduli with the applied strain-amplitude (i.e. assess the nonlinear damping seen in the experiments of Reed (2007) and Pearson (2008)). The material constants that are used in the following simulations are listed in Table 1. However, due to the lack of experimental studies that evaluate the interfacial properties between splats, those material constants have been chosen by trail-and-error to match the experimental results of strain-amplitude dependence of storage and loss moduli in magnesium aluminate spinel ceramic coatings by Pearson (2008). Therefore, one of the crucial challenges of the proposal microstructural cohesive zone model, which is the same for other exiting cohesive laws, is the identification of the associated material constants. Atomistic simulations of the debonding/sliding processes at the fault's interface could be effective and useful in identifying these material parameters. Furthermore, careful micro-deformation experiments on individual interfaces are an alternative expensive approach to establish the traction–separation curves in the normal and tangential directions. However, this is beyond the scope of the current study. It can be seen from the listed values of the critical separations, δ_m^{o} and δ_m^{f}, in Table 1 that they are in the expected micrometer range since the average splat's thickness is 2–10 μm as reported through the SEM images in Pearson (2008).

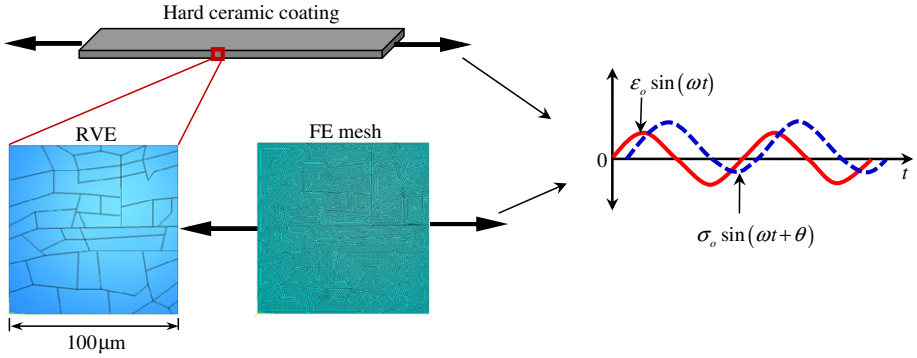

Fig. 8. Micromechanical analysis procedure showing a free standing ceramic coating, RVE with the splat structure, finite element mesh with cohesive zone elements at splat interfaces, applied strain, and obtained stress response.

Table 1
List of material constants.

Young's modulus	70 GPa	δ_N^o	0.1 μm	α_N	0.3
Poisson's ratio	0.22	δ_T^o	0.15 μm	α_T	0.3
K_N	7 GPa	δ_N^f	0.7 μm	μ	0.2
K_T	3 GPa	δ_T^f	1.05 μm	h	0.3 GPa
Y_o	0 GPa	B	0.3		

Fig. 9 shows the evolution of micro-cracks due to decohesion of interfacial faults at strain-amplitude of 300 μm (i.e. 300 micro-strains) and excitation frequency of 200 Hz (close to the resonant frequency of ceramic coatings) for 100 s (this is equivalent to 20,000 cycles). Although, this is much smaller than the total number of cycles that the ceramic coatings in Reed (2007) and Pearson (2008) are subjected to, which is in the range of five millions of cycles, these simulations will yield excellent assessment of the portion of energy dissipation due to damage and energy dissipation due to internal friction. Such assessment is crucial for the design and fabrication of ceramic coatings with higher levels of energy dissipation that suppress higher levels of unwanted vibrations and noise. It can be seen from the simulations in Fig. 9 that during the decohesion process, not many micro-cracks do propagate through the splats' bulk such that most of the applied energy is spent in the decohesion/separation process, sliding, and contact friction. Also, negligible widening of horizontal cracks is noticed.

Fig. 10(a) and (b) shows the evolution of dissipated energy due to damage and friction, respectively. The crucial observations from these figures are that the magnitude of damage dissipation energy is almost negligible to that of the frictional dissipation energy, and

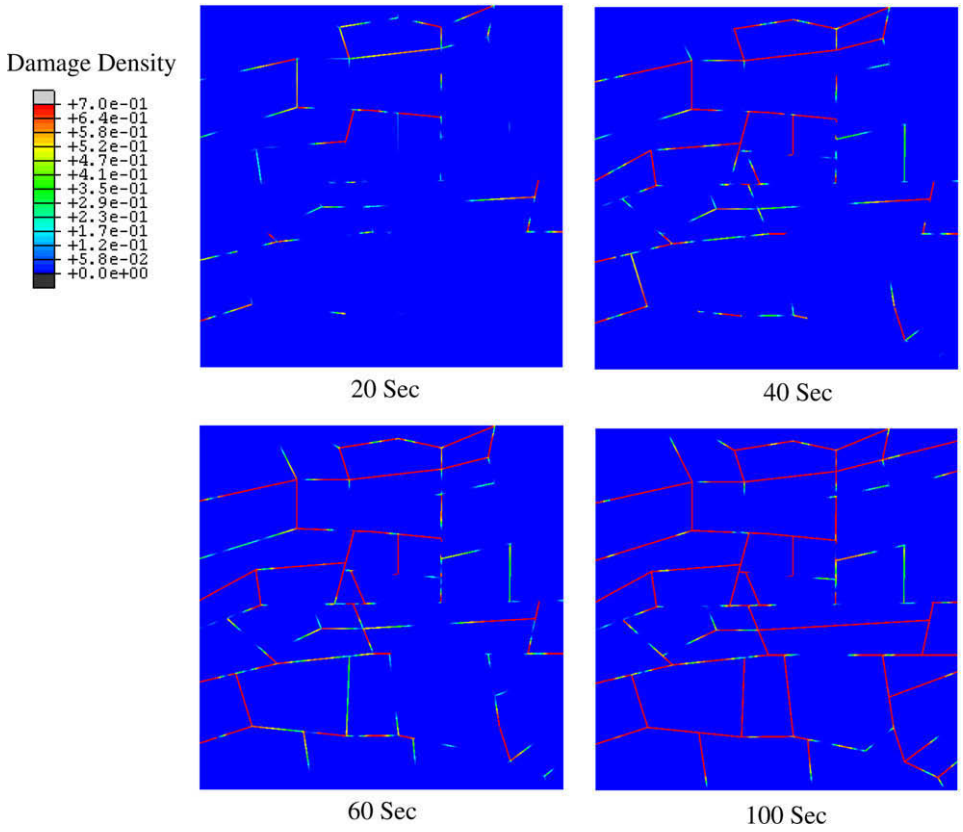

Fig. 9. Interfacial damage evolution (decohesion) at strain-amplitude 300 μm and frequency of 200 Hz.

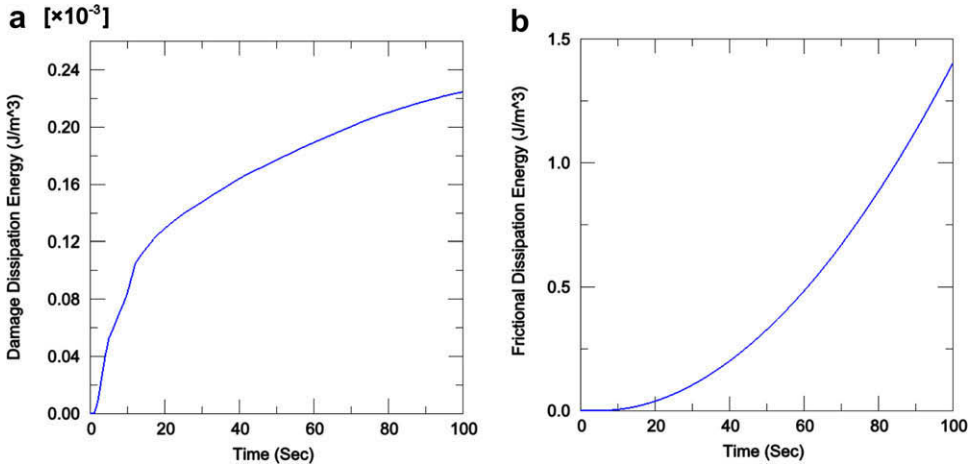

Fig. 10. Damage dissipation energy versus frictional dissipation energy due to decohesion and contact friction between splats' interfaces at strain-amplitude 300 μm and frequency of 200 Hz.

the rate of frictional dissipation energy keeps increasing with time whereas the rate of damage dissipation energy decreases with time and saturates at some point. Therefore, during the first few hundreds of cycles, majority of cohesive bonds are broken and contact friction is the main energy dissipation mechanism afterwards. In other words, energy dissipation due to damage evolution contributes to damping only at earlier stages of vibration. Thus, it can be concluded that higher splat density with enhanced frictional/sliding properties of splats' interfaces has a larger impact on energy dissipation and damping since more frictional interfaces are available for energy dissipation. This agrees well with the experimental observations of Shipton and Patsias (2003) and Pearson (2008). Moreover, it is noticed that when the RVE is under compression, the frictional energy dissipation is much higher than that in tension since in compression more plastic sliding and consequently contact friction occur between pre-existing and recursive faults (Pearson, 2008). As can be noticed from the microscopic image and the corresponding idealization in Fig. 3 that the majority of the interfaces are parallel to the applied strain-amplitude such that in tension most of the applied energy is spent stretching the splats and debonding the vertical interfaces, whereas in compression and upon interfacial debonding most of the energy is spent overcoming the friction between the splats along the horizontal and vertical interfaces. Fig. 11 shows the evolution of energy dissipated due to friction for decreasing values of the kinetic coefficient of friction, μ. It is noticed that even for a low value of $\mu = 0.01$, the frictional energy dissipation is several magnitudes higher than the energy dissipated due to damage (Fig. 10(a)) due to collective contact friction between the surfaces of pre-existing and recursive microstructural faults. Further, as strain-amplitude increases more surfaces of microstructural faults come into contact with each other in a progressive manner, which is the main reason for the observed amplitude-dependent internal friction (i.e. nonlinear damping) behavior seen in Figs. 12 and 13. These figures are obtained by repeating the RVE simulations with increasing strain-amplitudes, ε_o, are applied. Fig. 12 shows that the coating modulus, which is represented as the storage modulus, decreases with ε_o whereas Fig. 13 shows that the loss modulus, or equivalently the loss factor, increases with ε_o and runs through a distinct maximum and then decreases. This behavior agrees qualitatively well with the experimental results of Reed (2007) and Pearson (2008).

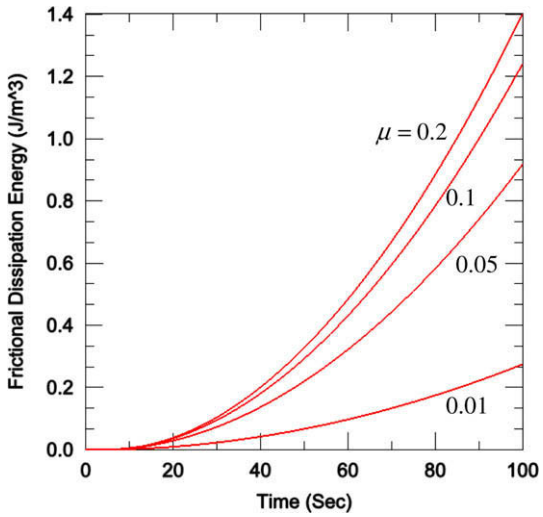

Fig. 11. Frictional dissipation energy due to contact friction between splats' interfaces for different values of the Coulomb friction coefficient at strain-amplitude 300 μm and frequency of 200 Hz.

It is noteworthy that according to the computational results from the current performed complex micromechanical modeling and simulations that the Iwan's spring-slider-mass analytical model (Iwan, 1966), which is based on the idea that energy dissipation is mainly attributed to internal friction, can be used effectively in predicting the nonlinear damping of hard ceramic coatings. In fact, with regard to computational efficiency, Iwan's model is recommended for implementation in numerical codes as compared to the current micromechanical approach which is computational expensive.

5. Conclusions

In this paper, a fundamental exploration of the main energy dissipation mechanism responsible for the experimentally observed amplitude-dependent nonlinear damping in plasma sprayed hard ceramic coatings is developed. In order to achieve this objective, a micromechanical cohesive zone model is developed within the laws of thermodynamic. This constitutive model explicitly models the decohesion, internal friction, and damage growth along the intra- and inter-microstructural faults or micro-cracks in the main building blocks of plasma sprayed coatings, which are the splats. This model is used to simulate the harmonic deformation response of an RVE description of the typical microstructure of plasma

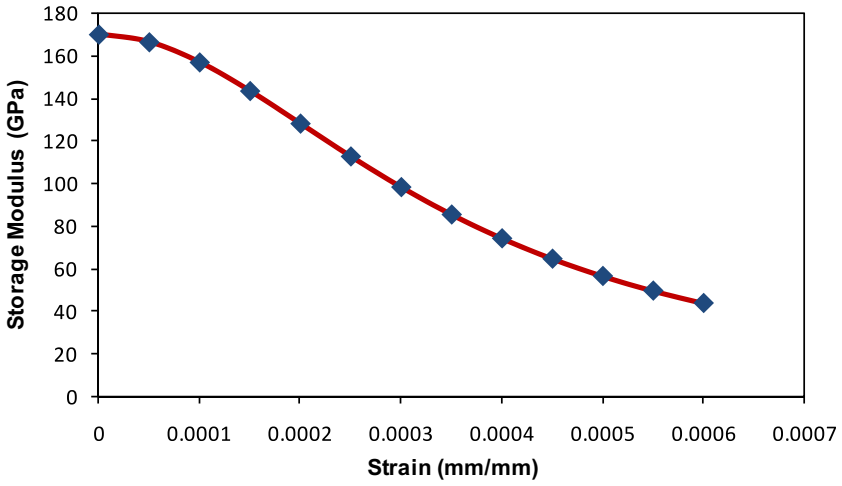

Fig. 12. Storage modulus as a function of amplitude at excitation frequency of 200 Hz.

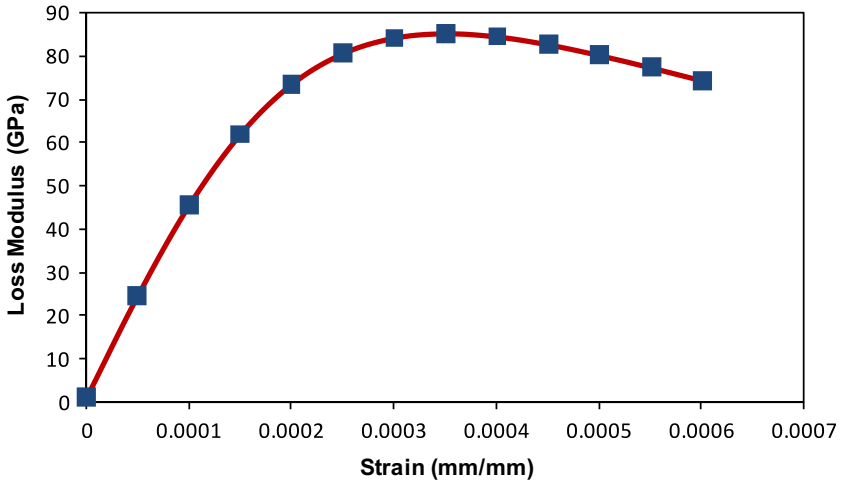

Fig. 13. Loss modulus as a function of amplitude at excitation frequency of 200 Hz.

sprayed coatings with recursive microstructural faults under isothermal strain-controlled excitations. Based on the micromechanical simulations the following conclusions are drawn:

(1) The main energy dissipation mechanism responsible for reducing vibration amplitudes in ceramic coated structures is internal friction due to gradual and increasing contact between the interfaces of microstructural recursive faults with increasing strain-amplitudes.
(2) Energy dissipation due to decohesion and damage growth is insignificant as compared to the energy dissipated due to Coulomb/contact friction. This suggests that for increasing levels of damping, one should increase the density of microstructural faults during the fabrication process by controlling the number (or size) of the splats through the coating thickness without sacrificing the integrity of the ceramic coating. Moreover, designing the interfacial properties of faults (i.e. an active rather than a passive approach) with higher levels of friction coefficient is desirable.
(3) As strain increases, more surfaces of microstructural faults come into contact with each other in a progressive manner, which is the main reason for the observed amplitude-dependent damping (i.e. nonlinear damping) behavior. The simulation results of variation of storage and loss moduli with strain-amplitude show qualitative satisfactory predictions of the observed behavior in the literature where the storage modulus decreases with amplitude, and the loss modulus increases with amplitude and runs through a distinct maximum and decreases afterwards.
(4) It can be seen from the simulations that during the decohesion process, micro-cracks do not propagate significantly through splats such that most of the applied energy is spent in the decohesion/separation process and plastic sliding friction. Also, negligible widening of horizontal cracks is noticed. This is in well agreement with the experimental observations made by Shipton and Patsias (2003) and Pearson (2008) which validate the proposed micromechanical modeling approach.
(5) It can be concluded that the Iwan's spring-slider-mass analytical model (Iwan, 1966), which attributes energy dissipation to internal friction only, can be effective in predicting nonlinear damping of hard ceramic coatings, and is more computational inexpensive as compared to the proposed micromechanical approach.

In future, several crucial issues need further investigation; namely: (1) Identification of the material parameters associated with the interfacial (cohesive zone) damage mechanics model is

a very important issue and a crucial challenge for these types of microstructural constitutive models. (2) More realistic microstructural RVEs that consider significant densities of faults between and inside splats and the existence of micro-pores will be generated in order to be able to quantitatively compare with the experimental data of Reed (2007) and Pearson (2008). (3) For more accurate assessment of the role of ceramic coatings in damping the mechanical vibrations in turbine engines and compressors, it is crucial to apply more realistic aerodynamic excitations and vibrations near the resonant frequency. (4) Wearing out of interfaces due to internal friction, which leads to decrease in the loss modulus, is expected at high number of cycles. This can be simulated by assuming a decaying function for the interfacial friction coefficient as a function of strain-amplitude. (5) Including three-dimensional effects is crucial for accurate estimation of the amount of energy dissipated due to internal friction. (6) The investigation and modeling of the temperature-dependence is important so that hard ceramic coatings can be ultimately used in hot and cold sections of the engine.

Acknowledgements

The authors acknowledge the financial support provided by Dr. Tommy George at the Turbine Engine Fatigue Facility at the Air Force Research Laboratory of the US Air Force Institute of Technology (AFIT) at WPAFB, Dayton, Ohio. Moreover, the first author acknowledges the fruitful discussions with Prof. William Baker, Dr. Shad Reed, and Mr. Oliver Easterday during his several visits to AFIT. The views expressed in this paper are those of the authors and do not reflect those of the US Air Force or Department of Defense.

References

ABAQUS, 2004. User Manual, Version 6.5, Habbitt, Karlsson and Sorensen, Inc., Providence, RI.

Abu Al-Rub, R.K., Voyiadjis, G.Z., 2003. On the coupling of anisotropic damage and plasticity models for ductile materials. Int. J. Solids Struct. 40, 2611–2643.

Barenblatt, G.I., 1959. The formation of equilibrium cracks during brittle fracture: general ideas and hypotheses, axially symmetric cracks. Appl. Math. Mech. 23, 622–636.

Blackwell, C., Palazotto, A., George, T.J., Cross, C.J., 2007. The evaluation of the damping characteristics of a hard coating on titanium. Shock Vib. 14, 37–51.

Camacho, G.T., Ortiz, M., 1996. Computational modeling of impact damage in brittle materials. Int. J. Solids Struct. 33, 2899–2938.

Chaboche, J.L., 2003. Damage mechanics. Compr. Struct. Integrity 2, 213–284.

Chaboche, J.L., Feyel, F., Monerie, Y., 2001. Interface debonding models: a viscous regularization with a limited rate dependency. Int. J. Solids Struct. 38, 3127–3160.

Coleman, B.D., Gurtin, M.E., 1967. Thermodynamics with internal state variables. J. Chem. Phys. 47 (2), 597–613.

Cross, K.R., Lull, W.R., Newmann, R.L., Cavanagh, J.R., 1973. Potential of graded coatings on vibration damping. J. Aircraft 10 (10), 689–691.

Dugdale, D.S., 1960. Yielding of steel sheets containing slits. J. Mech. Phys. Solids 8, 100–104.

Hutchinson, J.W., Evans, A.G., 2000. Mechanics of materials: top–down approaches to fracture. Acta Mater. 48, 125–135.

Ivancic, F.T., 2003. The Effect of a Hard Coating on the Damping and Fatigue Life of Titanium. M.Sc. Thesis, Air Force Institute of Technology, Dayton, OH.

Ivancic, F.R., Palazotto, A.N., 2005. Experimental considerations for determining the damping coefficients of hard coatings. J. Aerospace Eng. 18, 8–17.

Iwan, W.D., 1966. A distributed-element model for hysteresis and its steady-state dynamic response. J. Appl. Mech. 33, 893–900.

Kachonov, L.M., 1958. On the creep fracture time. Izv. Akad. Nauk USSR Otd. Tech. 8, 26–31 (in Russian).

Krajcinovic, D., 1983. Continuum damage mechanics. Appl. Mech. Rev. 37, 1–6.

Lakes, R.S., 1998. Viscoelastic Solids. CRC Press, Boca Raton, FL.

Lauwagie, T., Lambrinou, K., Patsias, S., Heylen, W., Vleugels, J., 2008. Resonant-based identification of the elastic properties of layered materials: application to air-plasma sprayed thermal barrier coatings. NDT & E Int. 41, 88–97.

Lemaitre, J., 1992. A Short Course in Damage Mechanics. Springer, New York.

Lemaitre, J., Chaboche, J.-L., 1990. Mechanics of Solid Materials. Cambridge University Press, London.

Needleman, A., 1990. An analysis of decohesion along an imperfect interface. Int. J. Fract. 40, 21–40.

Patel, R., Palazotto, A., 2004. Finite element method based model to study high cycle fatigue in turbine blades. ASCE J. Aerospace Eng. 17, 45–55.

Patsias, S., Saxton, C., Shipton, M., 2004. Hard damping coatings: an experimental procedure for extraction of damping characteristics and modulus of elasticity. Mater. Sci. Eng. A 370, 412–416.

Pawlowski, L., 1995. The Science and Engineering of Thermal Spray Coatings. Wiley, England.

Pearson, L.E., 2008. Vibration Analysis of Commercial Thermal Barrier Coatings. M.Sc. Thesis, Air Force Institute of Technology, Dayton, OH.

Reed, S.A., 2007. Development of Experimental, Analytical, and Numerical Approximations Appropriate for Nonlinear Damping Coatings. Ph.D. Dissertation, Air Force Institute of Technology, Dayton, OH.

Reed, S.A., Palazotto, A.N., Baker, W.P., 2007. An experimental technique for the evaluation of strain dependent material properties of hard coatings. Shock Vib. 14, 1–16.

Shipton, M., Patsias, S., 2003. Hard damping coatings: internal friction as the damping mechanism. In: Proceedings of the Eighth National Turbine Engine High Cycle Fatigue (HCF) Conference, Monterey, California, USA.

Tassini, N., Patsias, S., Lambrinou, K., 2006. Ceramic coatings: a phenomenological modeling for damping behavior related to microstructural features. Mater. Sci. Eng. A 442, 509–513.

Tassini, N., Lambrinou, K., Mircea, I., Bartsch, M., Patsias, S., Van der Biest, O., 2007. Study of the amplitude-dependent mechanical behavior of yttria-stabilised zirconia thermal barrier coatings. J. Eur. Ceram. Soc. 27, 1487–1491.

Torvik, P.J., 2009. Determination of mechanical properties of non-linear coatings from measurements with coated beams. Int. J. Solids Struct. 46, 1066–1077.

Xu, X.P., Needleman, A., 1994. Numerical simulations of fast crack growth in brittle solids. J. Mech. Phys. Solids 42, 1397–1434.